Ultra-broadband Passive Acoustic Metasurface for Wide-angle Carpet Cloaking

Hong-Tao Zhou [a], Wen-Xiao Fu [a], Yan-Feng Wang [a,*], Yue-Sheng Wang [a,†], Vincent Laude [b,**], and Chuanzeng Zhang [c]

[a] School of Mechanical Engineering, Tianjin University, Tianjin, 300350, China
[b] Institut FEMTO-ST, CNRS UMR 6174, Université Bourgogne Franche-Comté, Besançon 25030, France
[c] Department of Civil Engineering, University of Siegen, Siegen D-57068, Germany

*Corresponding author: wangyanfeng@tju.edu.cn, Yan-Feng Wang
†Corresponding author: yswang@tju.edu.cn, Yue-Sheng Wang
**Corresponding author: vincent.laude@femto-st.fr, Vincent Laude

Abstract

Acoustic metasurfaces can reshape a reflected wavefront rather arbitrarily, despite being much thinner than the wavelength, thus allowing on-demand wavefront modulation in a variety of applications. Recent passive metasurfaces, however, have suffered from bandwidth limitations, thus restricting their range of operation. In this work, we propose the systematic design of ultra-broadband passive metasurfaces by combining the broadband local reflection rule with an optimization method. The validation of the technique is demonstrated by fabrication and measurement of an ultra-broadband carpet cloak. Numerical and experimental results show that the relative bandwidth of the optimized carpet cloak, thinner than one fifth of the maximum wavelength, can exceed 93.33%, a value that is much larger than that of previous passive metasurfaces. Furthermore, multi-frequency pulse incidence tests reveal the excellent time-domain broadband characteristics of the metasurface over a wide range of angles of incidence. The proposed strategy opens a new route for the design of advanced passive metasurfaces for ultra-broadband wave manipulation and thus promotes practical applications of broadband acoustical devices.

Keywords: Acoustic metasurfaces; Carpet cloaking; Ultra-broad band; Wide angle; Inverse optimization design

1. Introduction

In recent years, metamaterials[1-3] have witnessed an unprecedented development for wave propagation control due to their marvelous wave modulation characteristics. With regard to the manipulation of acoustic waves, acoustic metamaterials[2, 3] have brought in various fantastic applications such as acoustic imaging[4], asymmetric transmission[5] and cloaking[6, 7], etc. However, it is still a challenge to design lightweight bulky metamaterials[8].

Thankfully, as a two-dimensional (2D) simplification of metamaterials, metasurfaces[8, 9] shake off the structural bulky limitation in a new wave manipulation route. By only implementing a single-layer of discrete microstructural units, one can manipulate sound wave propagation arbitrarily with a local phase and/or an amplitude modulation at the sub-wavelength scale[8]. In particular, plenty of thin or even ultra-thin metasurfaces have been designed for acoustic carpet cloaking[10-14]. These convex metasurfaces are placed on the ground to hide objects beneath them. However, because the acquired gradient phase based on the generalized Snell-law (GSL) depends acutely on frequency, it is quite difficult to achieve broadband modulation by passive metasurfaces compared with metamaterials[10, 13, 15]. The relative bandwidth of previously reported passive carpet cloaks[11, 12] thus varies from 7% to 36%.

As an exception, a gradient profile of effective sound velocity or refractive index has been employed to design pentamode metasurfaces[16-18]. Since its effective refractive index is almost a constant in a relatively wide frequency range, a pentamode metasurface[16-18] is generally suitable for broadband manipulation of acoustic waves in water. However, such a solution is hardly applicable to acoustic waves in air, since the density of air is much smaller than the density of solid media. In addition, it is possible to obtain a dispersionless phase response by using a simple groove structure[19]. With such a concept, however, it is difficult to reserve enough space for a curved carpet cloak because the groove depth has to increase with increasing height. Furthermore, several tunable[20-22] or active metasurfaces[3] have been put forward to enlarge the bandwidth. The regulation mechanisms considered are mainly based on tunable mechanical reconfiguration or multifield coupling[3]. Regrettably, they are still subject to frequency-dependent limitations, since different geometrical configurations are required at different frequencies. They thus would fail in case of a broadband incident pulse. Therefore, practical design strategies for passive broadband metasurfaces still remain scarce.

In view of the present narrow-bandedness of passive metasurfaces, we propose a systematic design for broadband passive metasurfaces by combining a broadband local reflection rule with parametric optimization[23]. The obtained broadband passive metasurface is verified by the design of an ultra-broadband carpet cloak. The fundamental unit of the metasurface is formed by stacking holes with different cross-sections. A reverse design technique based on an optimization algorithm is applied to find suitable structures. The total thickness of the unit-cell is limited to one fifth of the maximum wavelength. The phase shift of the unit-cell can be flexibly controlled by changing the geometrical parameters. Furthermore, we numerically and experimentally illustrate that the relative bandwidth of our reversely designed curved metasurface cloak can exceed 93.33%, which is much larger than that of the previously reported passive designs. Finally, a multi-frequency pulse test demonstrates the successful operation of the broadband passive metasurface over a wide-angle range in the time domain.

2. Broadband manipulation mechanism and inverse optimization design

Figure 1(a) shows a schematic diagram of a 2D curved metasurface for acoustic wavefront manipulation, where the reflected wave can be steered to any desired direction via an adequate phase gradient imparted by the metasurface. The broadband local reflection rule dominated by the phase distribution for the 2D curved metasurface can be expressed as follows

$$\Phi\left(f,x,z\right)=-\frac{2\pi f}{c_0}\left[\left(\sin\theta_r-\sin\theta_i\right)x+\left(\cos\theta_r+\cos\theta_i\right)z\right]+2D\pi, D\in\mathbb{Z},$$

(1)

where x and z are spatial coordinates of the curved metasurface and $\Phi(f,x,z)$ is the required phase distribution on the broadband metasurface; f and c_0 are the frequency and sound velocity, respectively; θ_i and θ_r represent the incidence and reflection angles, respectively; and $2D\pi$ is the periodic term of $\Phi(f,x,z)$. Eq. (1) indicates that the dependence of the phase function on the frequency is explicitly involved. A broadband metasurface can be realized if the phase distribution varies linearly with frequency. The detailed derivation of Eq. (1) can be found in the

Methods section. When we consider a broadband carpet cloak such as the one shown in Fig. 1(b), θ_i and θ_r should be equal at any position. Thus, Eq. (1) can be further simplified as

$$\Phi(f,x,z) = -\frac{4\pi z\cos\theta_i}{c_0} f + 2D\pi, D \in \mathbb{Z}, f \in [f_b, f_d],$$

(2)

where $[f_b, f_d]$ is the targeted broadband frequency range.

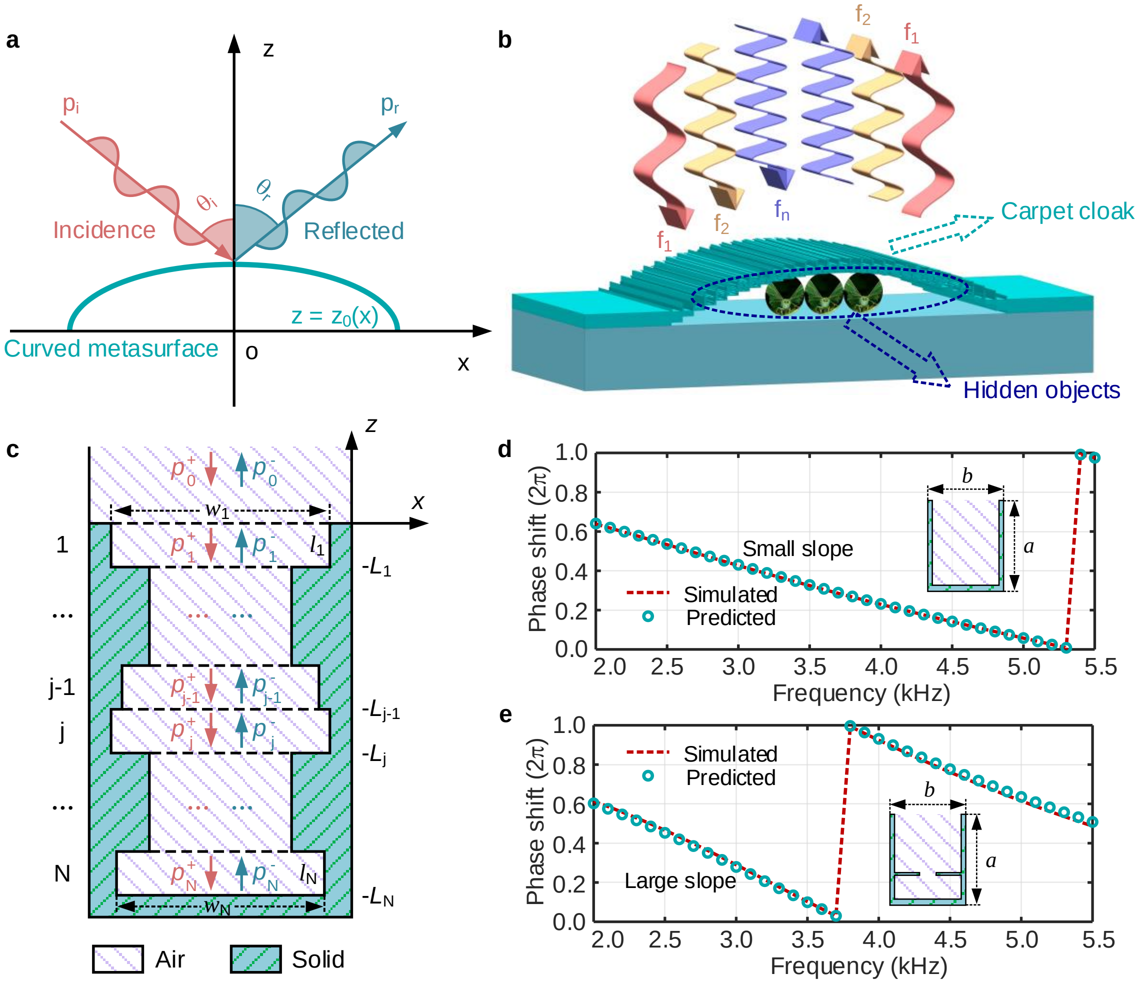

Fig. 1. *Schematic sketch of the ultra-broadband metasurface for carpet cloaking. (a) Illustration of a 2D curved metasurface for reflected wavefront manipulation. (b) Three-dimensional (3D) model of the broadband metasurface for carpet cloaking. With an incident broadband acoustic beam, the curved acoustic metasurface can mimic the reflection behavior of the flat ground. Acoustic waves are reflected at the angle of wave incidence so that the objects can be well hidden under the carpet cloak and protected from detection. (c) Schematic diagram of the stack-up unit-cell for acoustic wave modulation. (d) Holes with the same cross-sectional area maintain a phase shift changing linearly with frequency with a small slope. (e) Holes with*

abrupt changes in the cross-sectional area maintain a phase shift changing linearly with frequency with a large slope.

To obtain a linear variation of the phase shift, we propose a fundamental unit-cell formed by stacking holes with different cross-sections as shown in Fig. 1(c). The stack-up unit-cell has N layers containing air holes. The thickness and width of each layer are $l_j = L_j - L_{j-1} = L(1 \le j \le N, L_0=0)$ and $w_j(0 \le j \le \mathrm{N})$, respectively. We can obtain the reflection coefficient for the stack-up unit-cell with varying cross-sections by the transfer matrix method as

$$r = \left.\frac{p_0^-}{p_0^+}\right|_{z=0} = \frac{M_{21}+M_{22}}{M_{11}+M_{12}},$$

(3)

where $\begin{bmatrix} M_{11} & M_{12} \\ M_{21} & M_{22} \end{bmatrix} = M_1 M_2 \cdots M_\mathrm{N}$ is derived from the transfer matrix for sound pressure in the $(j\text{-}1)$th and jth layers with

$$M_j = \frac{1}{2}\begin{bmatrix} \left(1+w_j/w_{j-1}\right)\exp\left(ikL\right) & \left(1-w_j/w_{j-1}\right)\exp\left(-ikL\right) \\ \left(1-w_j/w_{j-1}\right)\exp\left(ikL\right) & \left(1+w_j/w_{j-1}\right)\exp\left(-ikL\right) \end{bmatrix}.$$

(4)

The detailed definitions and a derivation can be found in the Methods section. The reflected wave phase shift of the stack-up unit is obtained by evaluating the phase angle of the reflection coefficient r.

In order to analyze the phase shift of the stack-up unit, two typical cases are considered next. In order to ensure subwavelength operation of the metasurface, the height a and the width b of the unit-cell are set as $\lambda_0/5$ and $\lambda_0/6$, respectively, where λ_0 is the wavelength at 2 kHz. The thickness of each layer L is 1 mm and the total number of layers N is 32. In the first case, each layer has the same cross-section ($w_j = 0.88b, j \in [1,N]$). According to Eq. (3), the approximate solution for the predicted phase shift is $-2kNL$, consistent with the expression in Ref.[19]. A more precise value of the phase shift of the unit-cell is obtained by using the commercial finite-element software COMSOL Multiphysics. The simulated and predicted phase shifts are shown in Fig. 1(d). The results agree very well and show that the phase shifts change linearly with frequency. Hence, we may obtain linear phase shifts with different slopes just by changing the number of layers N. Since the height of the unit-cell remains in the subwavelength range, the slope change is relatively small. This type of unit cell is suitable for lower locations $z_0 < a$. For units placed at a higher location $z_0 \geq a$, we shall increase the slope by introducing an abrupt change in the cross-sectional area ($w_{23} = 0.22b$) as shown in Fig. 1(e). In this case, due to the abrupt change in the cross-section, an extra length ΔL must be taken into consideration[24]. The effective thickness of the contraction layer has to be corrected to $L' = L + \Delta L$ [24]. In Fig. 1(e), the simulated phase shift shows a larger slope than that in the case of Fig. 1(d) and the predicted phase shift fits the simulated result very well with the correction term $\Delta L = 0.63w_{23}$. Overall, the proposed stack-up units are expected to be appropriate for constructing a broadband carpet cloak.

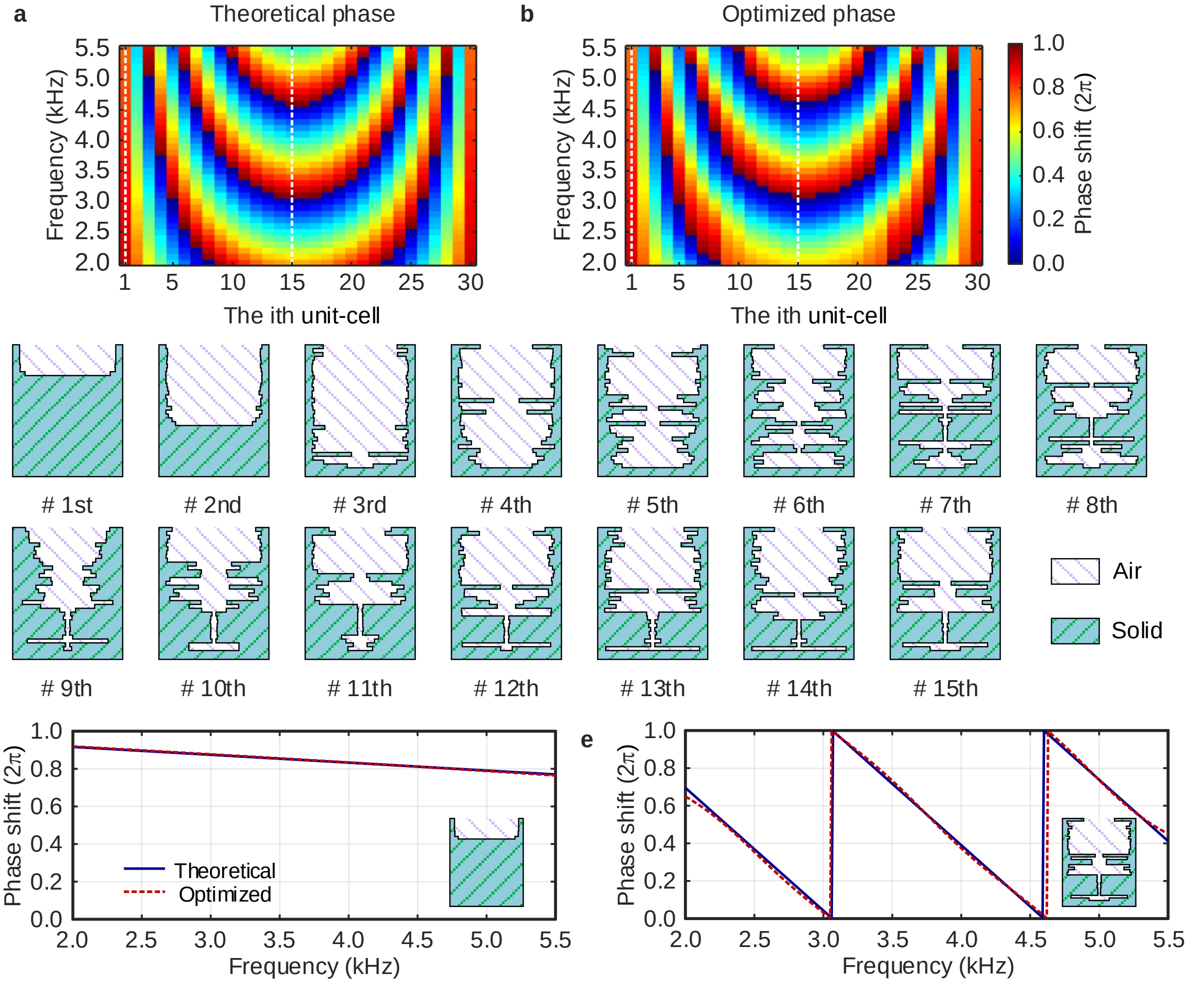

Fig. 2. *Optimized unit-cells and phase distributions of the ultra-broadband metasurface for carpet cloaking. (a-b) The theoretical and optimized phase distributions are shown for different unit-cells and frequencies, respectively, where the theoretical phase distributions are obtained by the broadband local reflection rule and the optimized phase distributions are obtained by the COMSOL Multiphysics software with optimal*

geometrical parameters. (c) The cross-sections of 15 optimized unit-cells, where the purple and green sections represent the air holes and solid structures, respectively, and the (31-i)th unit-cell have the same structure as the ith unit-cell. The linear phase shift as a function of frequency is shown in (d) for the 1st and in (e) for the 15th unit-cell.

Then we adopt parametric optimization to reversely design the unit-cells. The optimization problem at hand is described by

$$\text{Find :} \quad \mathbf{w}_m = \left[w_{m,1}, \cdots, w_{m,j}, \cdots, w_{m,N} \right], m \in [1, nc], N \in [1, nl],$$

(5)

$$\text{Minimizing :} \quad \varphi_{erro} = \sum_{f \in [f_b, f_d]} \left| \varphi(\mathbf{w}_m, N, f) - \left[-4\pi f z_0(x_m) \cos\theta_i / c_0 \right] \right| ,$$

(6)

$$\text{Subject to :} \quad l_{m,j} = 1\, mm, w_{m,j} \in [e, b-2e], e = a/20, j \in [1, N],$$

(7)

where nc and nl represent the number of the unit-cells and layers; $\mathbf{w}_m$, φ ($\mathbf{w}_\mathrm{m}$, N, f) and $z_0(x_m)$ denote the width parameter vector, reflected wave phase shift and height of the mth unit-cell, respectively; f_b and f_d are the upper and lower limits of the target frequency range; e is the minimum wall thickness. We construct the carpet cloak with a curved shape determined from an arc circle. 30 unit-cells ($nc = 30$) are used to build up the metasurface. The location $z_0(x_m)$ and the layer number nl of each unit-cell are listed in the Supplementary Materials. The height-to-thickness ratio of the curved metasurface is 3.26. A total of 36 discrete frequencies are chosen from the target frequency range ($f_b = 2$ kHz, $f_d = 5.5$ kHz). For parametric optimization, we used a genetic algorithm with continuous variables to find the optimal $\mathbf{w}_m$ for the stack-up units, where φ ($\mathbf{w}_\mathrm{m}$, N, f) is obtained by the COMSOL Multiphysics software. In order to accelerate convergence, the fitness function is calculated by

$$fitness = p_1 \mathrm{mean}[\varphi_{erro}] + p_2 \max[\varphi_{erro}] + p_3 \sum \max[\varphi_{erro}]_n,$$

(8)

where mean[*] and max[*] represent the average and maximum operations; $\sum \max[*]_n$ denotes the sum of the first n maximum values; p_1, p_2 and p_3 are the corresponding weight coefficients. We choose $n = 10$ and $p_1/p_2/p_3 =$ 1/1/10 in our calculations.

Figure 2(a) and 2(b) present the theoretical distribution based on the broadband local reflection rule only and the optimal one. It can be seen that the theoretical and optimal phases remain very close in a wide frequency range. The cross-sections of the optimized unit-cells are shown in Fig. 2(c). No abrupt changes are observed in the cross-sections of the 1st and 2nd unit-cell at $z_0 < a$, but one or more abrupt changes appear subsequently for the remaining unit-cells located at $z_0 \geq a$. This observation is consistent with the previous theoretical analysis. In Fig. 2(d) and 2(e), we also present the theoretical and optimized phase shifts versus frequency for the 1st and 15th unit-cells. The profiles of the phase shifts obtained by both methods are closely consistent. This fact confirms the feasible design of the present broadband metasurface carpet cloak.

3. Ultra-broadband cloaking in frequency domain

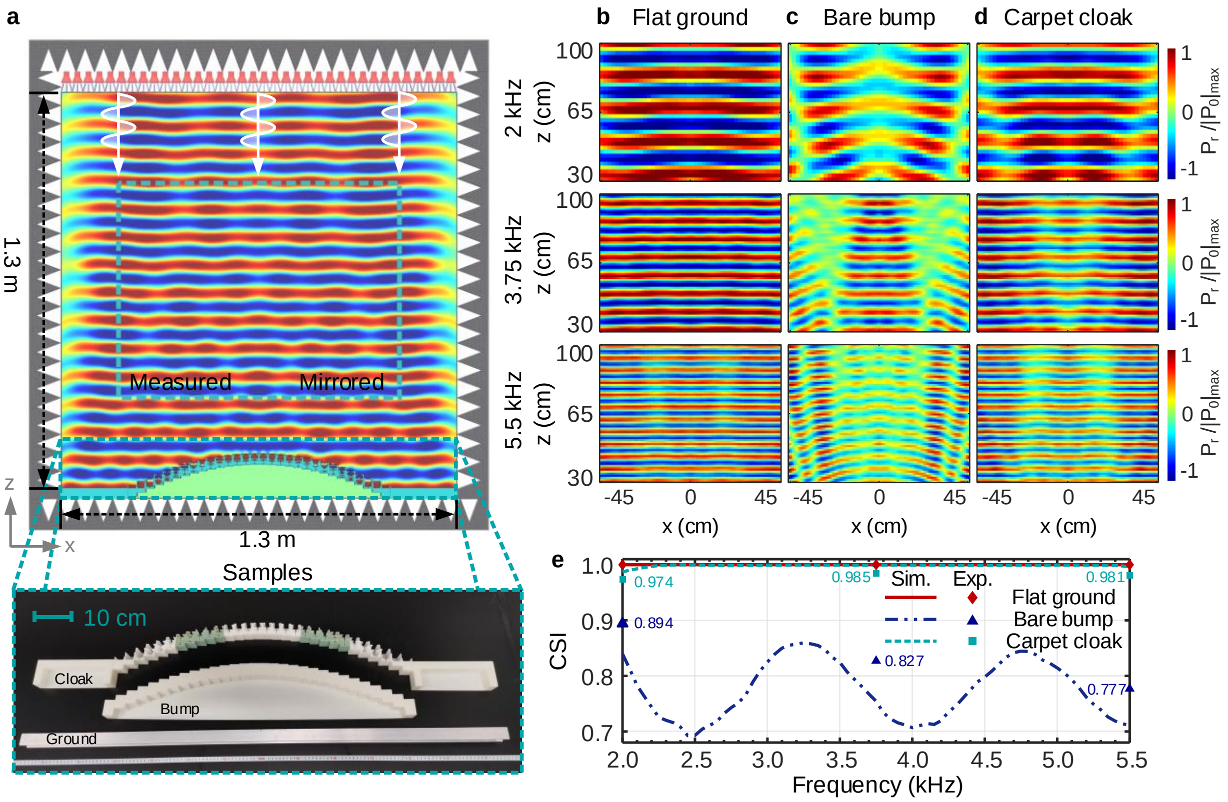

Fig. 3. *Experimental setup and measured results. (a) Schematic representation of the experimental setup and the fabricated samples of the flat ground, the bare bump and the carpet cloak. The measured normalized real part of the reflected pressure fields for the flat ground (b), the bare bump (c) and the carpet cloak (d) are shown at three incident wave frequencies: 2.0 kHz (1st row), 3.75 kHz (2nd row) and 5.5 kHz (3rd row). |P0|max, which denotes the maximum of the measured acoustic pressure amplitude without samples, equals*

1.86 Pa, 0.94Pa and 0.52 Pa for 2.0 kHz, 3.75 kHz and 5.5 kHz, respectively. The measured reflected wavefront phase is given in the Supplementary Materials. These plots contain the measured region and a mirrored region to cover a larger section. A video showing the corresponding simulated reflected pressure fields for different frequencies is presented in Video S1. (e) The quantitative analysis of the ultra-broadband metasurface carpet cloak is performed with the CSI.

To evaluate the ultra-broadband property of the designed metasurface for carpet cloaking, we constructed the experimental set-up shown in **Fig. 3**(a). A loudspeaker array excites plane acoustic waves with different frequencies. Three cases are measured: the flat ground, the bare bump, and the carpet cloak. Details of sample fabrication and experimental measurement are provided in the Methods section. The real parts of the reflected acoustic pressure fields at frequencies 2 kHz, 3.75 kHz and 5.5 kHz are presented in Fig. 3(b)-3(d), respectively. The reflected wavefront phase has also been measured and is shown in the Supplementary Materials. When the incident wave impinges normally on the bare bump, the reflected pressure field is significantly distorted, and the wavefronts are no longer continuous. The strong contrast in the reflected wave fields between the bare bump (see Fig. 3(b)) and the flat ground (see Fig. 3(c)) makes the object easily detected. On the contrary, when we cover the bump with our designed cloak, the disturbed pressure fields at different frequencies are effectively restored (see Fig. 3(d)) and the cloak redirects the wave as if it had been reflected on the flat ground. Thus, the designed metasurface can hide the object underneath efficiently. Simulated pressure fields for incident wave frequencies from 2 kHz to 5.5 kHz are provided in Video S1. Slight amplitude attenuations between measurements for the flat ground and the carpet cloak can be noticed, which may be mainly attributed to thermoviscous loss in the unit-cells. A detailed analysis is included in the Supplementary Materials.

To further characterize the broadband performance of the carpet cloak, cosine similarity (*CSI*) between two regions is introduced to precisely quantify stealth effectiveness[25]. The higher the value of *CSI* is, the better the stealth performance is. The *CSI* value is calculated as

$$CSI = \frac{\mathbf{P}^r \cdot \mathbf{P}^b}{\left|\mathbf{P}^r\right|\left|\mathbf{P}^b\right|} = \frac{\sum_{s=1}^{S}\sum_{t=1}^{T}\left(P_{st}^r \times P_{st}^b\right)}{\sqrt{\sum_{s=1}^{S}\sum_{t=1}^{T}\left(P_{st}^r\right)^2} \times \sqrt{\sum_{s=1}^{S}\sum_{t=1}^{T}\left(P_{st}^b\right)^2}}, \tag{9}$$

where $\mathbf{P}^r$ and $\mathbf{P}^b$ are the reflected wavefront phases off the flat ground and off the bump (with and without carpet cloak); the subscripts "*s*" and "*t*" denote the row and column of the observed area, respectively. Fig. 3(e) illustrates the variation of CSI_{cloak} between the carpet cloak and the flat ground as a function of the incident frequency. The results for CSI_{ground} and CSI_{bump} are also presented for comparison. It is found that CSI_{bump} oscillates around 0.77 with frequency, significantly lower than CSI_{cloak}, which is extremely close to the CSI_{ground} (=1) of the flat ground itself over the entire frequency band. Furthermore, the measured results for the above discussed three cases are also given in Fig. 3(e). The discrete measured values also indicate that CSI_{cloak} is significantly higher than CSI_{bump}. These simulated and experimental results illustrate that the present passive metasurface behaves as a carpet cloak with excellent broadband stealth performance. The relative bandwidth exceeds 93.33%, hence breaking the narrowband limitation of previously reported passive metasurfaces.

4. Cloaking under multi-frequency incident pulse

Another situation worth considering is the incidence of a multi-frequency pulse in the time domain. This allows us to check whether the designed passive metasurface can work well for a broadband incident source, a situation that is hardly handled by a tunable broadband metasurface cloak[20, 21]. Here, we chose the Gaussian pulse as the external random incident signal. The time history curves and the corresponding spectra in the frequency domain are shown in **Fig. 4**(a) and 4(b), respectively. The Gaussian pulses include either one or three tone frequencies f_c in their spectra. The transformed signal extends from 2 to 5.5 kHz with an amplitude larger than 10% of the maximum, which is suitable for verification of the broadband cloak[26].

Figure 4(c) and 4(d) show simulated snapshots under the incidence of a multi-frequency pulse in the time domain. The snapshots at $T = 10T_0$ show that the Gaussian pulse is incident as a plane wave (see the 1st column). Starting from the snapshot at $T = 30T_0$, it can be seen that the sound waves propagate backwards following specular reflection after hitting the flat ground (see the 2nd column). In contrast, the pulse signal spreads radially in the presence of the bump, making the object visible (see the 3rd column). When covered with the carpet cloak, however, the arched wavefronts are transformed into parallel planes again, mimicking the reflection characteristics of the flat ground (see the 4th column). Thus, the hidden object becomes effectively transparent and escapes detection. A complete video in the time domain is presented in Video S2.

In addition, to analyze further the performance of the cloak, we extract the time domain signals at points A, B and C. The signals measured at point B are shown in Fig. 4(e) and 4(f) for the three cases. The signals measured at points A and C are also provided in the Supplementary Materials. The incident and reflected pulses are easily distinguished from the time scale. The incident pulses are identical in all three cases. The phase of the acoustic wave reflected by the cloak almost coincides with that reflected by the flat ground, in strong contrast with the case of the bare bump. The slight decrease in the amplitude of the wave reflected by the cloak is presumably due to thermoviscous loss. In general, the carpet cloak exhibits distinguished time-domain broadband characteristics, and hence breaks the narrowband limitation of previously reported passive metasurfaces.

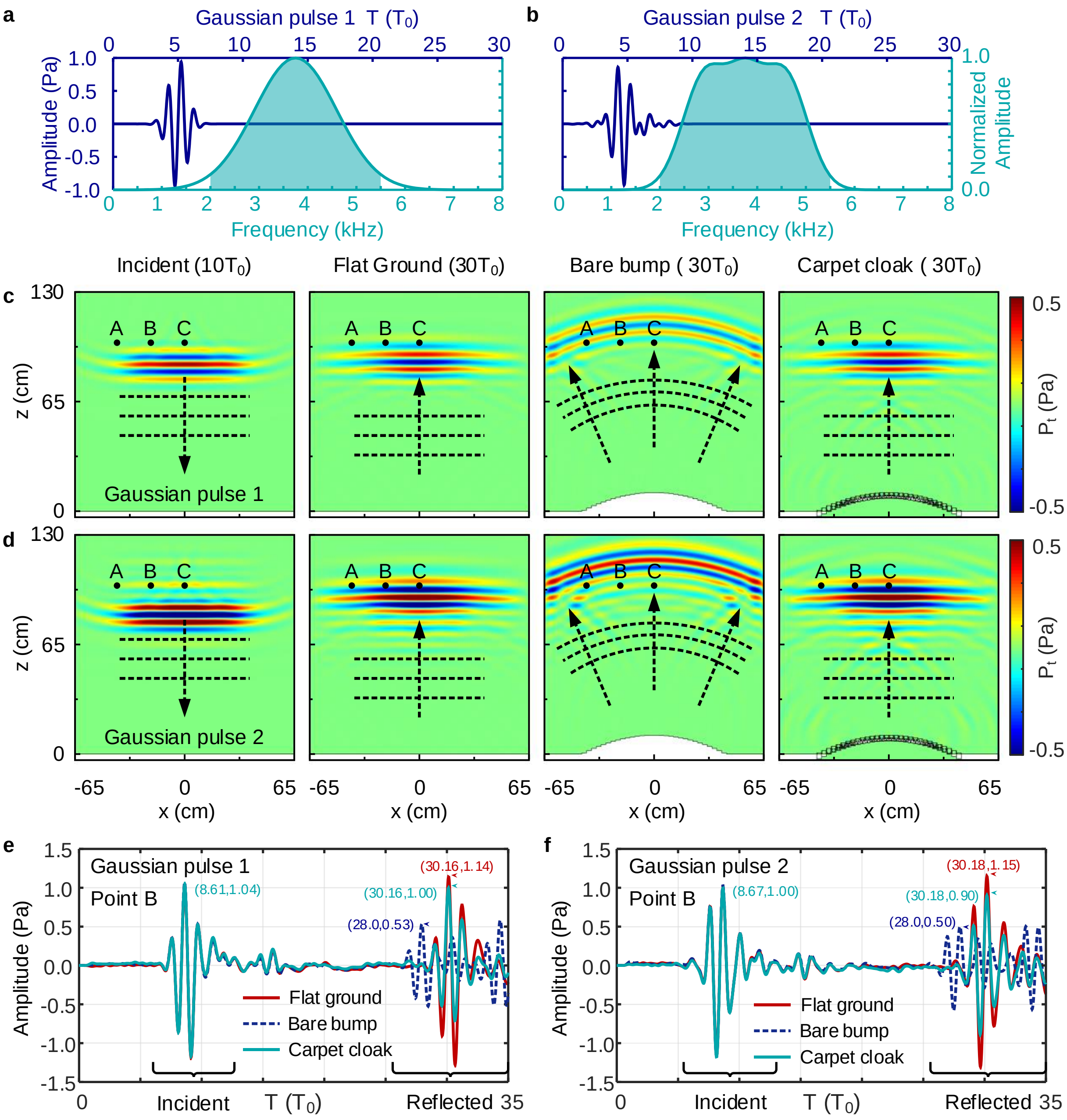

Fig. 4. *Time-domain broadband characteristics of the ultra-broadband carpet cloak. (a-b) Time-domain and frequency-domain plots of the two types of the incident Gaussian pulse signals. Instantaneous reflected pressure field snapshots are shown for Gaussian pulse 1 (c) and Gaussian pulse 2 (d). Four particular cases are presented: the snapshots of the incident signals at* $T = 10T_0$ *(the 1st column), the reflected signals by the flat ground (the 2nd column), the bare bump (the 3rd column), and the carpet cloak (the 4th column), at* $T = 30T_0$*. (e-f) The measured incident and reflected acoustic pressure signals at location B (-20 cm, 100 cm) are presented for three scenarios: the flat ground, the bare bump and the carpet cloak for incident Gaussian pulses 1 and 2, respectively. The measured signals at locations A (-40 cm, 100 cm) and C (0 cm, 100 cm) for the above three scenarios are presented in the Supplementary Materials.* T_0 *(0.2667 ms) is the period of the frequency of 3.75 kHz. A video showing the simulated dynamical incident and reflected pressure fields in the time domain is provided in Video S2.*

5. Broadband wide-angle cloaking

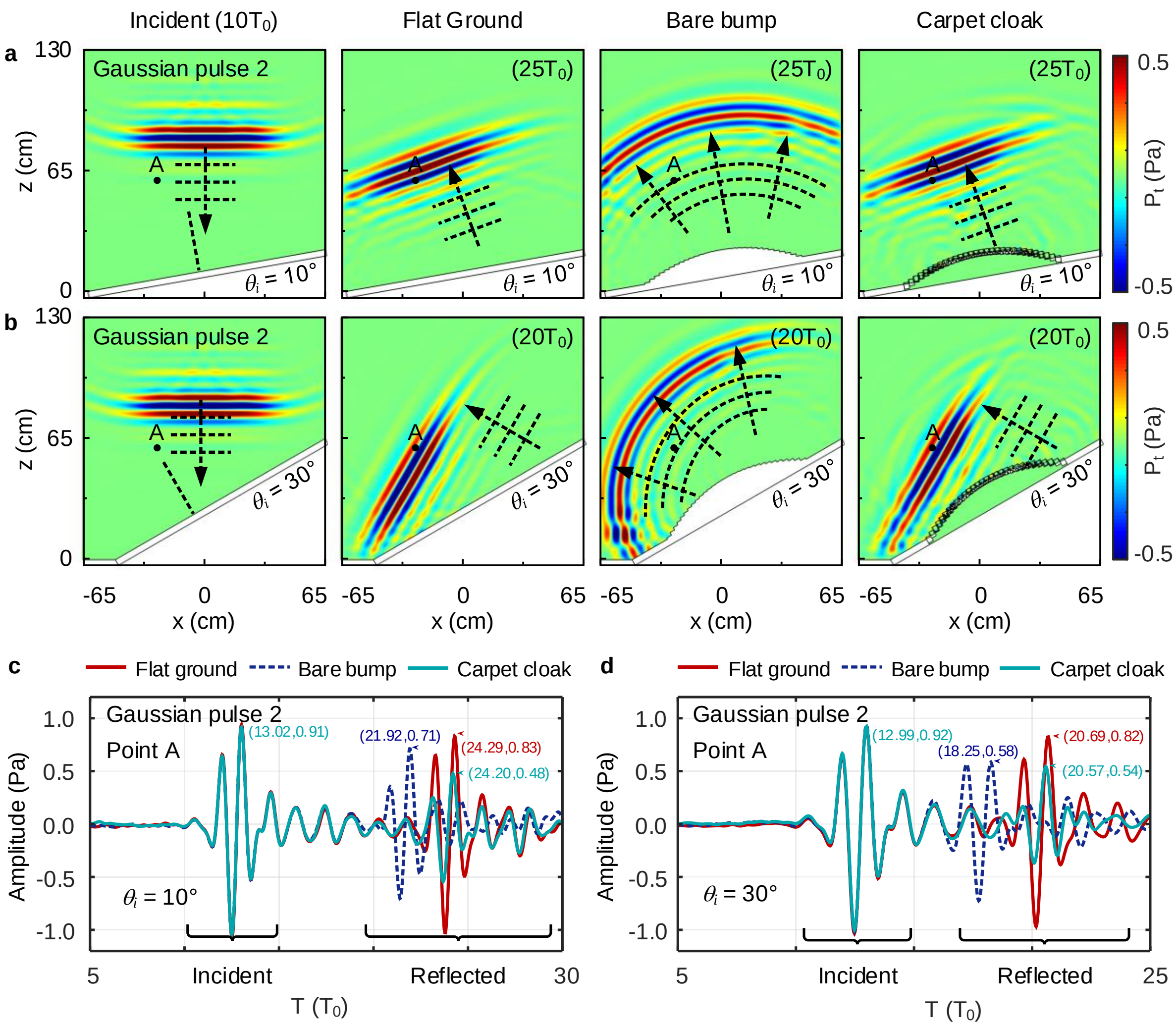

Fig. 5. *Ultra-broadband carpet cloak for wide-angle multi-frequency incident pulse. The time-domain snapshots are shown for the incident signal at $T = 10T_0$ (the 1st column), the signal reflected by the flat ground (the 2nd column), the bare bump (the 3rd column), and the carpet cloak (the 4th column). They are shown at $T = 25T_0$ for 10° oblique incidence (a) and at $T = 20T_0$ for 30° oblique incidence (b) of Gaussian pulse 2. (c-d) The measured incident and reflected acoustic pressure signals at location A (-25 cm, 60 cm) are presented for the three scenarios: the flat ground, the bare bump and the carpet cloak, for incident Gaussian pulse 2 for 10° (c) and 30° (d) oblique incidence. T0 (0.2667 ms) is the period of the frequency of 3.75 kHz. A video showing the simulated dynamical incident and reflected pressure fields in the time domain is provided in Video S3.*

Equation (2) indicates that the theoretical phase distribution for carpet cloaking also depends on the incident angle θ_i. It is still a challenge to achieve an omnidirectional metasurface for carpet cloaking. However, a wide-angle carpet cloak may be constructed. Since the phase is a sinusoidal function of the incidence angle θ_i, there is only a slight change in the theoretical phase distribution when θ_i varies around 0°. Therefore, the present metasurface also works for oblique incidence with a small angle ($\theta_i \leq 10°$). **Fig. 5**(a) shows the time-domain snapshots of the acoustic pressure fields for the flat ground, bare bump and carpet cloak, for 10° oblique incidence of Gaussian pulse 2. The three objects are inclined by an angle θ_i, and the acoustic signals are still incident from the negative direction of the z axis (see the 1st column). A similar specular reflection on the carpet cloak (see the 4rd column) and on the flat ground (see the 2nd column) can be observed for multi-frequency incident pulses, in stark contrast with the diffuse reflection by the bare bump (see the 3rd column). This means that the metasurface designed for normal incidence can still conceal objects for slightly oblique incidence.

When the incident angle becomes larger ($\theta_i > 10°$), the change in the theoretical phase distribution is $-4\pi f z_0(1-\cos\theta_i)/c_0$, a linear function of frequency. Hence, we just need to raise the height of the unit-cells designed for normal incidence, instead of redesigning them to achieve wide-angle carpet cloaking. The required height change is $\Delta z = z_0(1-\cos\theta_i)/\cos\theta_i$. Fig. 5(b) shows the corresponding time-domain results for 30° oblique incidence on the three objects. Excellent broadband stealth performance for the oblique incidence is observed. A video showing the simulated dynamical incident and reflected pressure fields in the time domain is provided in Video S3.

Besides, we extracted the time-domain signals at point A to analyze further the stealth performance of the wide-angle carpet cloak. Fig. 5(c) and 5(d) show the measured transient sound pressure fluctuations at point A for the three objects, for 10° and 30° oblique incidences, respectively. It can be seen that the acoustic pressure signal reflected by the bare bump is obviously different from that reflected by the flat ground. In contrast, although there is some attenuation in amplitude, which may be mainly attributed to thermoviscous loss in the unit-cells, the acoustic signal reflected by the carpet cloak is close to the case of the flat ground. A detailed analysis is included in the Supplementary Materials. Overall, the simulated and experimental results show an excellent broadband wide-angle stealth performance. In addition, we note that the invisibility effect gradually worsens as θ_i increases, owing to the curved geometry, and that a critical angle θ_i is determined by the maximum curvature of the metasurface[21].

6. Conclusions

In summary, we have systematically designed and experimentally demonstrated a passive ultra-broadband metasurface. The broadband design strategy is implemented based on a broadband local reflection rule. Meanwhile, an optimization method is applied to reversely design the desired metasurface. As an implementation example, a passive ultra-broadband carpet cloak with a thickness less than one fifth of the maximum wavelength was successfully realized with stack-up units. Numerical simulations and experimental measurements confirm that the relative bandwidth of the designed metasurface exceeds 93%, much larger than obtained with passive designs previously reported in the literature. Finally, the time-domain broadband characteristics of the present passive metasurface was demonstrated by the excellent performance of the cloak under a wide-angle multi-frequency incident pulse.

It should be noted that the operating bandwidth of a metasurface depends on the required broadband phase distribution function. From Eq. (1), the broadband local reflection rule indicates that the phase shift of each unit-cell should be a linear function of the incident frequency. Here, we define a dimensionless frequency-dependent factor $\gamma = \left| \frac{\partial \Phi(f, x, z)}{\partial f} \frac{c_0}{4\pi d} \right|$ to measure the difficulty of implementing a broadband reflective metasurface, where d is the thickness of the metasurface. The factor γ measures the change in the phase shift with frequency achieved by the unit-cell with fixed thickness. In this paper, the 15th unit-cell was placed at the highest location and we obtained $\gamma_{\max} = z_{\max} \cos\theta_i / d = 3.26$. This maximum value further determines the height-to-thickness ratio of the curved metasurface for normal incidence. The 15th unit-cell thus satisfies the theoretical phase shift in the frequency range 2-5.5 kHz, limiting the operation bandwidth. For a smaller value of γ, the available frequency range is larger. For example, γ is 2.43, 1.33 and 0.61 for the 8th, 4th and 2nd unit-cells, respectively; the associated frequency ranges are 1.5-5.8 kHz, 1-6.7 kHz and 1-10 kHz. Hence, the smaller the factor γ is, the easier the design of a broadband metasurface is.

In this paper, the broadband metasurface requires stacked-up unit-cells with different values of γ. When $\gamma < 1$, the fundamental unit-cell degenerates into the channel type, and the operating frequency range is rather wide. When $\gamma > 1$, the fundamental unit-cell evolves into a resonance structure. It is known that the bandwidth of a resonant unit-cell is generally narrow. However, the unit-cells in Fig. 2(c) have many different abrupt changes in cross-section and are similar to a series of resonators with multiple resonance frequencies. The arrangement gives rise to multiple resonances, and broadband modulation is obtained.

Finally, it should be noted that ultra-broadband passive metasurfaces can also be realized following other design principles, such as the ultra-broadband absorption metasurface[27]. If topology optimization[28-30] were combined with our concept, the relative bandwidth of the present passive metasurface may be further enlarged. In general, the present design concept may provide a bright future for practical applications of ultra-broadband acoustic devices in human lives.

7. Methods

2D Broadband Local Reflection Rule: As shown in Fig. 1(a), when the incident time-harmonic wave impinges on the metasurface, the incident and reflected acoustic pressure fields can be expressed as

$$p_i\left(f,x,z\right)=P_i\exp\left[-j\left(k\sin\theta_i x-k\cos\theta_i z\right)\right],$$

(10)

$$p_r\left(f,x,z\right)=P_r\exp\left[-j\left(k\sin\theta_r x+k\cos\theta_r z\right)\right],$$

(11)

where the common time-harmonic term $e^{-j\omega t}$ is omitted; P_i and P_r denote the incident and reflected pressure amplitudes, respectively; and $k=2\pi f/c_0$ is the wavenumber with frequency f and sound velocity c_0. Then the local acoustic pressure reflectance R can be calculated by

$$R\left(f,x,z\right)=p_r/p_i=P_r/P_i\exp\left\{-j\frac{2\pi f}{c_0}\left[\left(\sin\theta_r-\sin\theta_i\right)x+\left(\cos\theta_r+\cos\theta_i\right)z\right]\right\}.$$

(12)

Therefore, the broadband phase distribution $\Phi(f,x,z)$ on a curved metasurface, termed the 2D broadband local reflection rule, is obtained as

$$\Phi\left(f,x,z\right)=\arctan\left\{\frac{\mathrm{Im}\left[R\left(x,z\right)\right]}{\mathrm{Re}\left[R\left(x,z\right)\right]}\right\}$$

$$=-\frac{2\pi f}{c_0}\left[\left(\sin\theta_r-\sin\theta_i\right)x+\left(\cos\theta_r+\cos\theta_i\right)z\right]+2D\pi, D\in\mathbb{Z}.$$

(13)

Transfer Matrix of the Stack-up Unit-cell: Assuming that the plane wave hypothesis is valid in the stack-up unit-cell, as shown in Fig. 1(c), the acoustic pressures in the $(j$-1$)$th and jth layers can be expressed as

$$p_{j-1}^{+}\left(f,z\right)=P_{j-1}^{+}\exp\left[ik\left(z+L_{j-1}\right)\right],$$

(14)

$$p_{j-1}^{-}\left(f,z\right)=P_{j-1}^{-}\exp\left[-ik\left(z+L_{j-1}\right)\right],$$

(15)

$$p_{j}^{+}\left(f,z\right)=P_{j}^{+}\exp\left[ik\left(z+L_{j}\right)\right],$$

(16)

$$p_{j}^{-}\left(f,z\right)=P_{j}^{-}\exp\left[-ik\left(z+L_{j}\right)\right],$$

(17)

where P_j^{+} and P_j^{-} are the amplitudes of the incident and reflected waves in the jth layer. The velocity components along the z axis associated with these pressure fields determined by $v=\frac{i}{2\pi f\rho_0}\nabla p$ read

$$v_{j-1}^{+}\left(f,z\right)=\frac{1}{\rho_0 c_0}P_{j-1}^{+}\left(\omega\right)\exp\left[ik\left(z+L_{j-1}\right)\right],$$

(18)

$$v_{j-1}^{-}\left(f,z\right)=-\frac{1}{\rho_0 c_0}P_{j-1}^{-}\left(\omega\right)\exp\left[-ik\left(z+L_{j-1}\right)\right],$$

(19)

$$v_{j}^{+}\left(f,z\right)=\frac{1}{\rho_0 c_0}P_{j}^{+}\left(\omega\right)\exp\left[ik\left(z+L_{j}\right)\right],$$

(20)

$$v_j^-\left(f,z\right)=-\frac{1}{\rho_0 c_0}P_j^-\left(\omega\right)\exp\left[-ik\left(z+L_j\right)\right],$$

(21)

where ρ_0 is the density of air. Through the boundary conditions at the interfaces, the relations between the sound wave components in the $(j\text{-}1)$th and jth layers are further characterized by

$$P_{j-1}^+ + P_{j-1}^- = P_j^+\exp\left(ikL\right)+P_j^-\exp\left(-ikL\right),$$

(22)

$$w_{j-1}\left[P_{j-1}^+ - P_{j-1}^-\right]=w_j\left[P_j^+\exp\left(ikL\right)-P_j^-\exp\left(-ikL\right)\right],$$

(23)

Finally, the transfer matrix M_j of the sound pressure in the $(j\text{-}1)$th and jth layers can be derived by combining Eq. (22) and (23) as

$$M_j=\frac{1}{2}\begin{bmatrix}\left(1+w_j/w_{j-1}\right)\exp\left(ikL\right) & \left(1-w_j/w_{j-1}\right)\exp\left(-ikL\right)\\ \left(1-w_j/w_{j-1}\right)\exp\left(ikL\right) & \left(1+w_j/w_{j-1}\right)\exp\left(-ikL\right)\end{bmatrix},\ j\in\left[1,N\right].$$

(24)

Measurement Setup: The samples of our metasurface carpet cloak and bare bump are fabricated with the PolyJet and SLA 3D printing techniques. The base materials contain green ABS and white photopolymer to reduce the structural deformation. Their density and Young's modulus are around 1180 kg m^{-3} and 2.65 GPa, respectively. The sample of the flat ground is made of aluminum. All structures with plastic or metal materials are modeled as a rigid frame due to the high impedance mismatch between the material and air. It is noted that other materials with high acoustic impedance constrast with air, such as steel, glass, etc., could have been used to design passive ultra-broadband metasurfaces, so our choice is one of convenience. A photograph of the measurement setup is shown in the Supplementary Materials. An array of 36 loudspeakers (1-in., Hivi B1S) is used to generate plane acoustic waves. The samples and the loudspeaker array are placed at both ends of the waveguide system with the height of 40 mm, fastened closely by two parallel acrylic plates with the thickness of 20 mm. Wedge-shaped porous foams are installed at the boundaries of the waveguide system for minimizing sound reflections.

Measurements in Frequency Domain: We first use a computer with the software PULSE LABSHOP to generate a continuous sound wave signal at a single frequency (e.g. 2 kHz, 3.75

kHz or 5.5 kHz). The acoustic signal is then diverted into two branches, where one branch is directly connected to the Input and Output Module (Type 3160-A-042, Brüel & Kjær) as a reference signal, while the other is amplified by a Power Amplifier (Krohn-Hite 7500) and is played with the loudspeaker array. A stepper motor control system is used to move a 1/8-inch microphone (Type 4138-A-015, Brüel & Kjær) to scan the pressure field in a rectangular region of 46 cm × 70 cm with a step size of 2 cm at 2 kHz and 1 cm at 3.75 kHz and 5.5 kHz. The total pressure field is retrieved by recording the magnitude and the phase at different spatial positions. The reflected pressure field is then obtained by subtracting the two pressure fields with and without sample.

Measurements in Time Domain: the experimental set-up is the same as that in Fig. 3(a). We select a transient wave excitation instead of a monochromatic source. A Gaussian pulse of the form $p\sum_{c=1}^{n}\left[\sin\left(2\pi f_c t\right)\right]\exp\left[-(t\text{-}5\mathrm{T}_0)^2/\delta^2\right]_{\max}$ is applied to drive the loudspeaker array, where $p_{\max}$ is the amplitude normalization coefficient; f_c denotes the center frequency; T_0 is the period corresponding to the frequency $\left(f_b+f_d\right)/2$ (3.75 kHz) and δ is used to adjust the pulse duration. Here, we select one and three values of f_c as the external random incident signals, where the parameters ($p_{\max}, f_c, \delta$) are (1 Pa, 3.75 kHz, T_0) for Gaussian pulse 1 and (0.53 Pa, 2.9/3.75/4.6 kHz, $1.9\mathrm{T}_0$) for Gaussian pulse 2. A set of individual time-domain signals are recorded at specific points, A, B and C in Fig. 4. Several measurements are performed and averaged to increase the signal-to-noise ratio.

Numerical Simulations: Numerical simulations are conducted with the 'Pressure Acoustics Module' in the commercial finite-element software COMSOL Multiphysics 5.4a. A triangular mesh is used with quadratic Lagrange elements, and the maximum element size is chosen as $\lambda_0/100$ and $\lambda_0/30$ for the areas inside and outside the unit-cells, respectively. Plane wave radiation boundary conditions are applied in the finite-element models to eliminate wave reflections on the external boundaries. To calculate the phase shifts of the unit-cells in Fig. 2, the solid material is assumed to be rigid; and the density and acoustic velocity of air are 1.21 kg m^{-3} and 343 m s^{-1}, respectively. Periodic boundary conditions are applied on the left and right sides. In order to ensure wavefront phase synchronism between the metasurface and the flat ground, the phase shift of the unit-cell as a function of frequency is obtained by referring the reflected phase to the flat ground. For the full wave simulation in Fig. 3, a uniform background pressure field serves as the incident wave in the frequency-domain calculations. For time-domain calculations in Fig. 4 and Fig. 5, the wave source is chosen as an incident pressure field with a Gaussian distribution in space under the plane wave radiation boundary condition.

Data availability

Data will be made available upon reasonable request. This is due to further, ongoing research in this field within this team.

CRediT authorship contribution statement

Hong-Tao Zhou: Conceptualization, Methodology, Validation, Investigation, Formal analysis, Software, Data Curation, Writing - original draft, Writing - review & editing. **Wen-Xiao Fu**: Software, Data Curation, Writing - review & editing. **Yan-Feng Wang**: Supervision, Funding acquisition, Conceptualization, Methodology, Formal analysis, Writing - review & editing. **Yue-Sheng Wang**: Supervision, Funding acquisition, Conceptualization, Methodology, Writing - review & editing. **Vincent Laude**: Funding acquisition, Writing - review & editing. **Chuanzeng Zhang**: Writing - review & editing.

Declaration of competing interest

The authors declare no competing financial interests.

Acknowledgements

This work is supported by National Natural Science Foundation of China (Grant Nos. 11991032, 11972246, 12072223, 11991031, 12021002). V. L. would like to thank the support from the EIPHI Graduate School (contract ANR-17-EURE-0002).

References

[1] N.I. Zheludev, Y.S. Kivshar, From metamaterials to metadevices, Nat. Mater. 11 (2012) 917-924. http://dx.doi.org/10.1038/nmat3431.

[2] S.A. Cummer, J. Christensen, A. Alu, Controlling sound with acoustic metamaterials, Nat. Rev. Mater. 1 (2016) 126230. http://dx.doi.org/10.1038/natrevmats.2016.1.

[3] Y.-F. Wang, Y.-Z. Wang, B. Wu, W. Chen, Y.-S. Wang, Tunable and active phononic crystals and metamaterials, Appl. Mech. Rev. 72 (2020) 040801. http://dx.doi.org/10.1115/1.4046222.

[4] J. Zhu, J. Christensen, J. Jung, L. Martin-Moreno, X. Yin, L. Fok, X. Zhang, F.J. Garcia-Vidal, A holey-structured metamaterial for acoustic deep-subwavelength imaging, Nat. Phys. 7 (2011) 52-55. http://dx.doi.org/10.1038/nphys1804.

[5] B.-I. Popa, S.A. Cummer, Non-reciprocal and highly nonlinear active acoustic metamaterials, Nat. Commun. 5 (2014) 3398. http://dx.doi.org/10.1038/ncomms4398.

[6] J. Li, J.B. Pendry, Hiding under the carpet: A new strategy for cloaking, Phys. Rev. Lett. 101 (2008) 263501. http://dx.doi.org/10.1103/PhysRevLett.101.203901.

[7] D. Torrent, J. Sanchez-Dehesa, Acoustic cloaking in two dimensions: A feasible approach, New J. Phys. 10 (2008) 063015. http://dx.doi.org/10.1088/1367-2630/10/6/063015.

[8] B. Assouar, B. Liang, Y. Wu, Y. Li, J.-C. Cheng, Y. Jing, Acoustic metasurfaces, Nat. Rev. Mater. 3 (2018) 460-472. http://dx.doi.org/10.1038/s41578-018-0061-4.

[9] N. Yu, P. Genevet, M.A. Kats, F. Aieta, J.-P. Tetienne, F. Capasso, Z. Gaburro, Light propagation with phase discontinuities: Generalized laws of reflection and refraction, Science 334 (2011) 333-337. http://dx.doi.org/10.1126/science.1210713.

[10] H. Esfahlani, S. Karkar, H. Lissek, J.R. Mosig, Acoustic carpet cloak based on an ultrathin metasurface, Phys. Rev. B 94 (2016) 014302. http://dx.doi.org/10.1103/PhysRevB.94.014302.

[11] M. Dubois, C. Shi, Y. Wang, X. Zhang, A thin and conformal metasurface for illusion acoustics of rapidly changing profiles, Appl. Phys. Lett. 110 (2017) 151902. http://dx.doi.org/10.1063/1.4979978.

[12] X. Wang, D. Mao, Y. Li, Broadband acoustic skin cloak based on spiral metasurfaces, Sci. Rep. 7 (2017) 11604. http://dx.doi.org/10.1038/s41598-017-11846-1.

[13] F. Ma, Y. Xu, J.H. Wu, Shell-type acoustic metasurface and arc-shape carpet cloak, Sci. Rep. 9 (2019) 8076. http://dx.doi.org/10.1038/s41598-019-44619-z.

[14] C. Faure, O. Richoux, S. Felix, V. Pagneux, Experiments on metasurface carpet cloaking for audible acoustics, Appl. Phys. Lett. 108 (2016) 064103. http://dx.doi.org/10.1063/1.4941810.

[15] Y. Yang, H. Wang, F. Yu, Z. Xu, H. Chen, A metasurface carpet cloak for electromagnetic, acoustic and water waves, Sci. Rep. 6 (2016) 20219. http://dx.doi.org/10.1038/srep20219.

[16] Y. Chen, G. Hu, Broadband and high-transmission metasurface for converting underwater cylindrical waves to plane waves, Phys. Rev. Appl. 12 (2019) 025601. http://dx.doi.org/10.1103/PhysRevApplied.12.044046.

[17] Y. Chu, Z. Wang, Z. Xu, Broadband high-efficiency controllable asymmetric propagation by pentamode acoustic metasurface, Phys. Lett. A 384 (2020) 126230. http://dx.doi.org/10.1016/j.physleta.2019.126230.

[18] Y. Tian, Q. Wei, Y. Cheng, Z. Xu, X. Liu, Broadband manipulation of acoustic wavefronts by pentamode metasurface, Appl. Phys. Lett. 107 (2015) 221906. http://dx.doi.org/10.1063/1.4936762.

[19] Y.-F. Zhu, X.-Y. Zou, R.-Q. Li, X. Jiang, J. Tu, B. Liang, J.-C. Cheng, Dispersionless manipulation of reflected acoustic wavefront by subwavelength corrugated surface, Sci. Rep. 5 (2015) 10966. http://dx.doi.org/10.1038/srep10966.

[20] S.-W. Fan, S.-D. Zhao, L. Cao, Y. Zhu, A.L. Chen, Y.-F. Wang, K. Donda, Y.-S. Wang, B. Assouar, Reconfigurable curved metasurface for acoustic cloaking and illusion, Phys. Rev. B 101 (2020) 024104. http://dx.doi.org/10.1103/PhysRevB.101.024104.

[21] H.-T. Zhou, S.-W. Fan, X.-S. Li, W.-X. Fu, Y.-F. Wang, Y.-S. Wang, Tunable arc-shaped acoustic metasurface carpet cloak, Smart Mater. Struct. 29 (2020) 065016. http://dx.doi.org/10.1088/1361-665X/ab87e4.

[22] X.S. Li, Y.F. Wang, A.L. Chen, Y.S. Wang, An arbitrarily curved acoustic metasurface for three-dimensional reflected wave-front modulation, J. Phys. D-Appl. Phys. 53 (2020) 15. http://dx.doi.org/10.1088/1361-6463/ab7327.

[23] J. Li, C. Shen, A. Diaz-Rubio, S.A. Tretyakov, S.A. Cummer, Systematic design and experimental demonstration of bianisotropic metasurfaces for scattering-free manipulation of acoustic wavefronts, Nat. Commun. 9 (2018) 1342. http://dx.doi.org/10.1038/s41467-018-03778-9.

[24] D.T. Blackstock, Fundamentals of Physical Acoustics, Wiley & Sons Ltd, New York, 2000.

[25] Y. Zhu, J. Hu, X. Fan, J. Yang, B. Liang, X. Zhu, J. Cheng, Fine manipulation of sound via lossy metamaterials with independent and arbitrary reflection amplitude and phase, Nat. Commun. 9 (2018) 1632. http://dx.doi.org/10.1038/s41467-018-04103-0.

[26] Y. Chen, M. Zheng, X. Liu, Y. Bi, Z. Sun, P. Xiang, J. Yang, G. Hu, Broadband solid cloak for underwater acoustics, Phys. Rev. B 95 (2017) 180104. http://dx.doi.org/10.1103/PhysRevB.95.180104.

[27] F. Ma, M. Huang, Y. Xu, J.H. Wu, Bilayer synergetic coupling double negative acoustic metasurface and cloak, Sci. Rep. 8 (2018) 5906. http://dx.doi.org/10.1038/s41598-018-24231-3.

[28] H.-W. Dong, S.-D. Zhao, P. Wei, L. Cheng, Y.-S. Wang, C. Zhang, Systematic design and realization of double-negative acoustic metamaterials by topology optimization, Acta Mater. 172 (2019) 102-120. http://dx.doi.org/10.1016/j.actamat.2019.04.042.

[29] J. Rong, W. Ye, Multifunctional elastic metasurface design with topology optimization, Acta Mater. 185 (2020) 382-399. http://dx.doi.org/10.1016/j.actamat.2019.12.017.

[30] J. Jung, S. Goo, J. Kook, Design of a local resonator using topology optimization to tailor bandgaps in plate structures, Mater. Des. 191 (2020) 108627. http://dx.doi.org/10.1016/j.matdes.2020.108627.